

Quantum Frequency Conversion for Ytterbium Ion Based Quantum Repeaters

by

Ryan A. Clark

Department of Electrical and Computer Engineering
Duke University

Date: _____

Approved:

Jungsang Kim, Supervisor

Richard B. Fair

Daniel J. Gauthier

Thesis submitted in partial fulfillment of the requirements for the degree of
Master of Science in the Department of Electrical and Computer Engineering
in the Graduate School of Duke University
2012

ABSTRACT

Quantum Frequency Conversion for Ytterbium Ion Based
Quantum Repeaters

by

Ryan A. Clark

Department of Electrical and Computer Engineering
Duke University

Date: _____

Approved:

Jungsang Kim, Supervisor

Richard B. Fair

Daniel J. Gauthier

An abstract of a thesis submitted in partial fulfillment of the requirements for
the degree of Master of Science in the Department of Electrical and Computer
Engineering
in the Graduate School of Duke University
2012

Copyright © 2012 by Ryan A. Clark
All rights reserved except the rights granted by the
Creative Commons Attribution-Noncommercial Licence

Abstract

Quantum key distribution systems represent a proven method to obtain fundamentally secure communication channels. However, the loss of entangled photons which create the encryption key limit the distance over which the systems are useful. Quantum repeaters have been used to increase the distance over which entangled photons can be transmitted. The most successful quantum repeaters entangle information between trapped ions and single photons and through the use of entanglement swapping protocols, relay the encryption keys over large distances. A requirement of these quantum repeaters is the ability to work in the telecom wavelengths (1310 nm or 1550 nm), where standard silica fibers exhibit low loss. With the majority of ions emitting in the ultraviolet and visible spectrum, and ytterbium in particular emitting at 369.5 nm, a conversion process is then needed that can translate the photons from 369.5 nm to the telecom band while preserving the entangled state. The experiment presented here details the first stage of a nonlinear frequency conversion setup that uses strong pump light to enable the conversion of 369.5 nm photons to 708 nm. The efficiency of the conversion process is analyzed to determine the optimum system parameters, with an initial single pass conversion efficiency of 0.20% achieved. Noise introduced during the nonlinear conversion process is examined to determine the effect it presents on the communication channel.

Contents

| | |
|---|-------------|
| Abstract | iv |
| List of Figures | vi |
| List of Abbreviations and Symbols | vii |
| Acknowledgements | viii |
| 1 Introduction | 1 |
| 2 Scalable quantum communication using trapped ytterbium ion based quantum repeaters | 5 |
| 2.1 Ion/Photon entanglement and entanglement swapping | 6 |
| 2.2 Difference frequency mixing in nonlinear crystalline materials | 12 |
| 2.3 Raman scattering and parametric fluorescence noise in crystalline media | 16 |
| 3 Experimental Overview of multi-stage UV to NIR quantum frequency converter | 19 |
| 3.1 772nm pump creation via second harmonic generation | 21 |
| 3.1.1 SHG Results | 23 |
| 3.2 Difference Frequency Generation of 708 nm Intermediate Frequency . | 26 |
| 3.2.1 DFG Results | 28 |
| 4 Analysis of Raman Scattering Noise in Lithium Niobate | 34 |
| 5 Conclusions | 41 |
| Bibliography | 44 |

List of Figures

| | | |
|-----|---|----|
| 2.1 | Ytterbium 171 energy level diagram | 7 |
| 2.2 | Ion/photon frequency entangled qubit. | 8 |
| 2.3 | Ion/photon polarization entangled qubit. | 9 |
| 2.4 | Ion/photon time bin entangled qubit. | 10 |
| 2.5 | Entanglement swapping via dual ion/photon entanglement. | 12 |
| 2.6 | Noise processes in nonlinear crystals | 17 |
| 3.1 | Two stage frequency conversion layout | 21 |
| 3.2 | Second harmonic generation layout | 24 |
| 3.3 | SHG temperature tuning bandwidth | 25 |
| 3.4 | SHG conversion | 26 |
| 3.5 | DFG layout for 369.5 nm to 708 nm conversion | 31 |
| 3.6 | DFG temperature tuning curve | 32 |
| 3.7 | DFG conversion efficiency | 33 |
| 4.1 | Measured $X(ZZ)\bar{X}$ Raman spectrum of PPLN | 36 |
| 4.2 | Stokes and anti-Stokes spectrum of PPLN crystal | 37 |
| 4.3 | Anti-Stokes scattering noise measurement layout | 39 |
| 4.4 | Noise measurements for 3 different center frequencies | 40 |

List of Abbreviations and Symbols

Abbreviations

The following abbreviations are used throughout this thesis.

| | |
|------|------------------------------------|
| DFG | Difference Frequency Generation |
| EDFA | Erbium Doped Fiber Amplifier |
| PPLN | Periodically Poled Lithium Niobate |
| QKD | Quantum Key Distribution |
| QPM | Quasi-Phase Matching |
| SHG | Second Harmonic Generation |
| Yb | Ytterbium (Ionized Species 171) |

Acknowledgements

In contrast to the Wizard of Oz where Dorothy lifts the curtain to reveal a sole individual behind the complex wizard that they had been seeking, lifting the curtain of my experiments reveals a large group of people who have contributed in knowledge, experience, and support. My advisor Dr. Jungsang Kim has provided the basis for the research I have performed, and has greatly improved my understanding of the field of quantum information. I would like to thank Dr. Peter Maunz for his ability to explain the most technical of details in a form that I could comprehend. Post docs Taehyun Kim and So-young Baek have been indispensable when I encountered obstacles that I saw no way around. Professor Dan Gauthier's knowledge and expertise allowed me to bypass some deadend paths and shortcut to solutions. And I must acknowledge the graduate students who provided assistance whenever I needed it, including Kyle McKay, Rachel Noek, and Emily Mount. Aside from educational and experimental support, I would like to thank my parents for encouraging me in any and all of my endeavors. My girlfriend Hannah Guilbert has helped me in more ways than she can ever imagine, including learning a deeper insight of quantum physics. And for their ability to distract me from the research process when it becomes overwhelming, I am grateful for my dog Qubit and her sister Emmy.

1

Introduction

A question that has perplexed society for centuries is how access to privileged information can be limited to parties that have proper authentication. Conventional methods involve the creation of an encryption key, that when applied to a message, renders it incomprehensible to anyone without the encryption key. This encryption method allows sent messages to be viewed by any observer, but understood only by someone who possesses the key. Examples of this type of encryption can be found in simple form or in computationally complex form such as the RSA encryption used in classified government communications [1]. The security, however, of these types of encryption methods hinges on the security of the shared encryption key. For example, the RSA encryption scheme relies on the computational difficulty in factoring very large numbers, a problem which has no known efficient algorithm. Brute force methods to find the prime factors of large numbers can take a prohibitively long time, scaling exponentially with the key length, thus making it computationally secure.

Despite their complexity, there still exist flaws in current encryption methods. Shor's factoring algorithm provides the framework for exponentially faster factoring through the use of quantum computing [2]. Even with modern technologies, the

security of current encryption methods relies on trust between sending and receiving parties. Not only is the security of the encryption method not guaranteed, there is no feedback if an eavesdropper gains even a fraction of the message. If the key is used numerous times, as in many encryption methods, not only can the initial data be compromised, but any further data sent.

Thus, there is a need for a provably secure encryption method that alerts the parties involved when the key may have been exposed. To this end, a method of encryption using quantum mechanics has been developed called quantum key distribution (QKD). There exist numerous protocols, but the basics revolve around the sharing of entangled particles that exhibit a strong correlation in certain degrees of freedom, regardless of the distance separating them. The entangled particles are distributed over a quantum communication channel to their respective parties, and each particle received represents a packet of information. By sending many particles, a long encryption key can be assembled. If an eavesdropper were to listen in onto the channel and try to perform a measurement to determine the contents of the key, a perceptible change would occur alerting the communicating parties that some information was leaked. This is due to the random errors that the eavesdropper must inject due to not knowing the basis in which the photons were sent. Commercially available QKD systems offer the benefits of secure communication, but they are limited in the distance over which they are effective. Typical telecommunication systems employ amplifiers to boost the signal over long distance fiber, but this scheme fails due to a property called the "no cloning" theorem which states that arbitrary quantum states cannot be copied.

A solution to this is a quantum repeater that can temporarily store quantum information and, through the use of entanglement swapping, purify and send that information. At the heart of quantum repeater is a quantum memory, a device that can retain quantum information and not lose it to the environment. There are nu-

merous choices for quantum memories, but certain conditions must be fulfilled for theoretical and practical purposes. The quantum memory must have a coherence time longer than the time needed for all logic and communication operations to be completed or the information will be corrupted. Furthermore, since numerous quantum memory devices are needed, repeatable fabrication technologies are paramount to the success of their implementation. Any variances between systems would require new control systems, prohibiting large scale use. Of the current technologies available, trapped ions represent the best options due to their identical nature and stable energy levels [3].

In spite of their advantages, trapped ions have several disadvantages that make them non-ideal for QKD systems. There are numerous practical considerations such as the ultra-high vacuum systems along with laser cooling needed to shield the ion from interactions with the environment to provide long coherence times. A key fundamental issue is the fact that most ions of interest have energy level spacing on the order of several eV. This energy spacing requires optical manipulation in the ultraviolet or visible which poses a problem: most optical communication devices have poor performance at these wavelengths. The most efficient way to transmit information over long distances is through fiber optics, which is composed of silica core glass. Standard wavelengths used for telecom fiber optics include 1310 nm and 1550 nm because these correspond to low absorption ranges of fiber. At shorter wavelengths, the light undergoes increased Rayleigh scattering causing higher losses. While the absorption coefficient for telecom wavelengths is on the order of 0.2 dB/km, it increases from 400 dB/km to over 1000 dB/km in the UV [4]. Overcoming the high loss of entangled particles is one key obstacle in creating a viable quantum repeater.

The challenge then becomes how to translate information carrying photons in the UV/visible regime to some telecom wavelength. The most conventional means to convert wavelengths is through nonlinear optics, where multiple wavelengths mix

to create a new wavelength. Various groups have demonstrated frequency conversion schemes that retain entanglement for quantum systems, including frequency upconversion from 1550 nm to 840 nm to allow for better detection [5] as well as downconversion from 740 nm to 1550 nm in the interest of allowing rubidium ions to work as memories in quantum repeaters [6]. The span of conversion has been limited thus far, and only visible to IR conversion processes have been performed. For ions that emit in the UV, such as ytterbium, multiple conversion stages are needed to prevent noise from overriding the signal.

In an effort to realize a quantum memory using trapped ytterbium ions, the following experiment has been designed that converts the 370 nm light from the ytterbium ion to a wavelength suitable for long distance transmission. The overall system requires two primary stages, the first converting the 370 nm output from the ytterbium ion to 708 nm and the second performing the final conversion of the 708 nm intermediate signal to 1310 nm. In this thesis, an overview of how trapped ions are used in a quantum repeater will be given, along with background on frequency conversion processes in non-centrosymmetric materials. The design of the experiment is then discussed, with results from the first stage including conversion efficiency and an investigation of noise, followed by an analysis on the implications this experiment holds for quantum repeaters using trapped ytterbium ions as memory elements.

Scalable quantum communication using trapped ytterbium ion based quantum repeaters

Quantum information systems differ from classical systems in that they exhibit a phenomena called superposition, where they can occupy more than one discrete state at a given time. In digital communication systems using two possible levels, a binary system, a unit of information can either be a 0 or a 1. With quantum information, however, a binary system can assume multiple values simultaneously, which can be written as $|\Psi\rangle = a|0\rangle + b|1\rangle$ where $|a|^2$ and $|b|^2$ represent the probability of being in the 0 or 1 state, respectively. This two state quantum system is referred to as a quantum bit, or qubit, and forms the basis for quantum communication.

Numerous types of systems are capable of carrying quantum information, from trapped neutral atoms [7] and trapped ionized atoms [8], to artificial atoms like quantum dots [9] and nitrogen vacancies in diamond [10]. Trapped ionized atoms interact minimally with their environment, unlike most artificial atom implementations, allowing them to possess long decoherence times which is ideal for quantum memories [3]. They do, however, allow local interactions due to Coulombic forces with other

ions if trapped in the same potential, allowing local gates to be performed[11]. Factors affecting the choice of different ion species include the complexity of the internal energy level structure, the energy spacing of the transitions of interest, the ion mass, and a host of other criteria. A good choice due to its microwave accessible hyperfine splitting, minimal energy levels (meaning minimal lasers needed for manipulation), and not too extreme energy level spacing is ytterbium 171 (denoted here as simply Yb).

2.1 Ion/Photon entanglement and entanglement swapping

The energy level diagram for Yb is given in Fig. 2.1 with only the relevant levels shown for clarity. Hyperfine splitting is responsible for the 12.6 GHz separation of the lowest ground state level (the $^2S_{1/2}, F = 0, m_F = 0$) from the other three $^{1/2}S_{1/2}$ levels, as well as for the 2.1 GHz separation of the $^2P_{1/2}, F = 0$ state from the three $^2P_{1/2}, F = 1$ states. Transitions between different levels can be performed via optical or microwave probing with a specific frequency. For instance, applying a microwave field at 12.6 GHz can transfer the population from the $^2S_{1/2}, F = 0, m_F = 0$ state to the $^2S_{1/2}, F = 1, m_F = 0$ state, called Rabi flopping. If an electron is in an excited state (i.e. in one of the $^2P_{1/2}$ levels), it will decay to one of the ground $^2S_{1/2}$ and emit a photon. This emitted photon has: a frequency determined by the energy difference of the state transitions, a polarization governed by the change in m_F , and a creation time corresponding to the spontaneous emission time. These three attributes can be used to entangle the information from an ion into a photon. All of the photons emitted from Yb will have an output near 369.5 nm, which is the energy spacing from the excited state to the ground state. Transitions from other levels will have higher or lower energies due to the hyperfine and Zeeman splitting, but these deviations will be on the order of several gigahertz at most.

Entanglement between a photon's frequency and the ion's energy levels can be

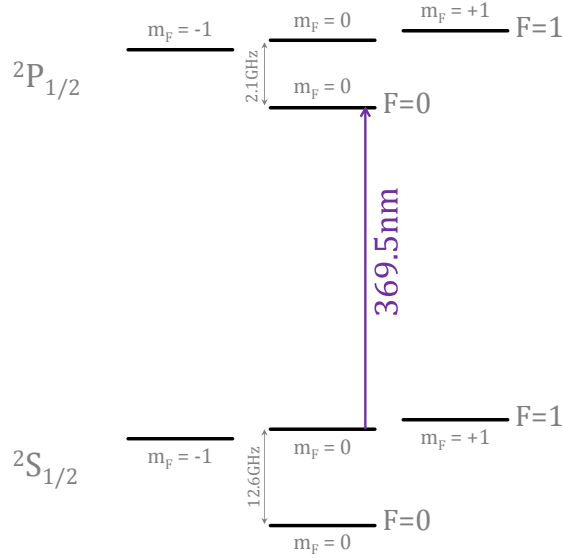


FIGURE 2.1: The relevant energy level structure of ytterbium 171. The ground state separation in the $^1/2S_{1/2}$ and $^2P_{1/2}$ is provided by hyperfine splitting. The fundamental energy level spacing resides in the UV at 369.5 nm.

generated in several ways, with one example shown in Fig. 2.2 [12]. The ion is prepared such that the electron is in the $^2S_{1/2}, F = 1, m_F = +1$ state. When 369.5 nm light is incident on the ion, the electron is excited to the $^2P_{1/2}, F = 1, m_F = +1$ state. The electron will decay probabilistically to one of three ground states, either the $F = 1, m_F = 0$, the $F = 1, m_F = +1$, or the $F = 0, m_F = 0$. Transition to the fourth ground state is forbidden due to the selection rules that prohibit a $\Delta F = 0$ and $\Delta m_F = \pm 2$. Of the three possible transitions, only the ones ending in a state with $m_F = 0$ will have the same polarization. Thus, by filtering the output with a polarization filter, two outcomes are possible, a transition to the $^2S_{1/2}, F = 1, m_F = 0$ (the $|1\rangle$ state), or a transition to the $^2S_{1/2}, F = 0, m_F = 0$ (the $|0\rangle$ state) with a 12.6 GHz larger frequency. Which energy level transition occurs is unknown unless the photon or ion are probed, thus resulting in the ion and photon becoming entangled. This three level quantum structure with two possible output

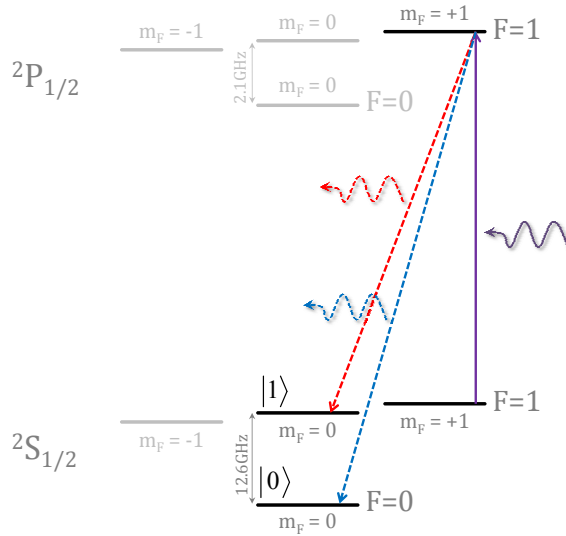


FIGURE 2.2: Entanglement of an ion and a photon using the photon’s frequency. With the ion prepared in the ${}^2S_{1/2}, F = 1, m_F = +1$ state, a laser excites the ion to the ${}^2P_{1/2}, F = 1, m_F = +1$ state where it will spontaneously decay. Using a polarization filter, only two outcomes are possible, either a transition to the ${}^2S_{1/2}, F = 1, m_F = 0$ state (denoted as the $|1\rangle$ state) or a transition to the ${}^2S_{1/2}, F = 0, m_F = 0$ state (denoted as the $|0\rangle$ state). A transition to the $|0\rangle$ state results in a 12.6 GHz larger frequency.

states is called a quantum bit, or qubit.

In much the same way as in the frequency qubit scheme, polarization and creation time can be entangled as well. For a polarization qubit (Fig. 2.3), the ion is prepared in the ${}^2S_{1/2}, F = 0, m_F = 0$ state and excited to the ${}^2P_{1/2}, F = 1, m_F = 0$ state. By using a polarization filter, only two possible outcomes may occur, either a transition to the ${}^2S_{1/2}, F = 1, m_F = -1$ $|0\rangle$ state with the photon having σ^+ polarization or a transition to the ${}^2S_{1/2}, F = 1, m_F = +1$ $|1\rangle$ state with σ^- polarization. A time bin qubit [13] (Fig. 2.4) starts with the ion prepared in a superposition of the ${}^2S_{1/2}, F = 1, m_F = 0$ $|1\rangle$ state and the ${}^2S_{1/2}, F = 0, m_F = 0$ $|0\rangle$ state. Light is applied to the ion that excites only the ${}^2S_{1/2}, F = 0, m_F = 0$ $|0\rangle$ state to the ${}^2P_{1/2}, F = 1, m_F = 0$ state. After an appropriate time has passed, a microwave

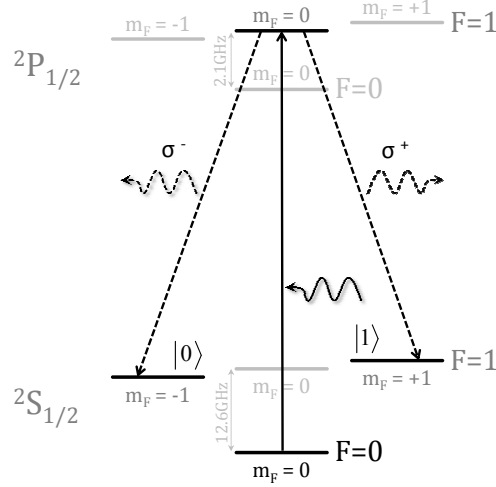


FIGURE 2.3: Entanglement of an ion and a photon using the photon’s polarization. The ion is prepared in the ${}^2S_{1/2}, F = 0, m_F = 0$ state, and a laser excites it to the ${}^2P_{1/2}, F = 1, m_F = 0$ state. With a polarization filter, there are two detectable decay transitions, one to the ${}^2S_{1/2}, F = 1, m_F = -1$ energy level with a σ^- polarization the other to the ${}^2S_{1/2}, F = 1, m_F = +1$ energy level with a σ^+ polarization.

pulse is applied that swaps the population of the $|0\rangle$ and $|1\rangle$ levels. Light is then reapplied to excite the electron from the ${}^2S_{1/2}, F = 0, m_F = 0$ $|0\rangle$ state to the ${}^2P_{1/2}, F = 1, m_F = 0$ state. If a photon was emitted in the first time bin, the ion must have been in the $|0\rangle$ state. If the photon was emitted in the second time bin, the ion would have been in the $|1\rangle$ state.

Thus, it has been shown how an ion, an ideal quantum memory component, can be entangled with a photon, a good carrier of information. The emitted photon, however, is not ideal for long distance transmission due to its ultraviolet wavelength which undergoes greatly increased Rayleigh scattering in optical fibers leading to losses of over 1000 dB/km [4]. At this level of loss, communication would take an exorbitant amount of time even over distances as short as several hundred meters. Even if the ion emitted in the telecommunications band, the loss still amounts to

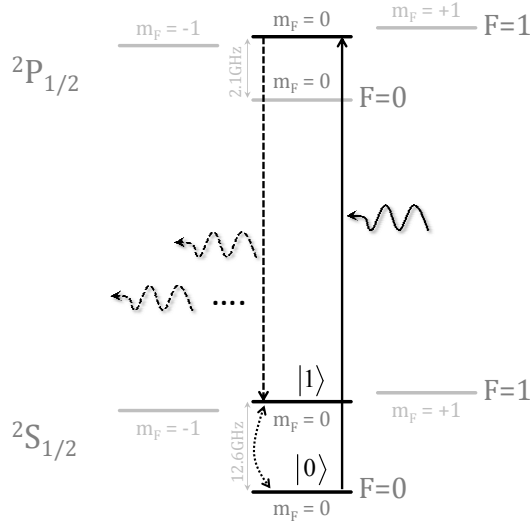


FIGURE 2.4: Entanglement of an ion and a photon using the photon’s creation time. The ion is prepared in a superposition of the ${}^2S_{1/2}, F = 0, m_F = 0$ state and the ${}^2S_{1/2}, F = 1, m_F = 0$ state, and then the ${}^2S_{1/2}, F = 0, m_F = 0$ is excited to the ${}^2P_{1/2}, F = 1, m_F = 0$ level. With a polarization filter, only light from the transition to the ${}^2S_{1/2}, F = 1, m_F = 0$ is collected. After a period of time, the population of the ${}^2S_{1/2}, F = 0, m_F = 0$ and ${}^2S_{1/2}, F = 1, m_F = 0$ levels are swapped using Rabi flopping. Again, the ion is then excited to the ${}^2P_{1/2}, F = 1, m_F = 0$ level and allowed to decay to the ${}^2S_{1/2}, F = 1, m_F = 0$ state. If the photon was emitted in the first time frame, the ion was in the ${}^2S_{1/2}, F = 0, m_F = 0$ $|0\rangle$ state, and if it was emitted in the second time frame, it was in the ${}^2S_{1/2}, F = 1, m_F = 0$ $|1\rangle$ state

0.2 dB/km, which would limit communication to tens of kilometers. To achieve long distance communication, a solution is needed that can circumvent this high loss. In standard optical based telecommunication systems, amplifiers are installed along the fiber that boost the optical signal strength. This method fails for quantum systems because any arbitrary quantum state cannot be cloned [14], and any gain in signal is accompanied by an equal gain in noise.

A theoretical solution to this problem is a quantum repeater [15], which is a device that transmits quantum information without making a measurement on it. Underlying the operation of a quantum repeater is the concept of entanglement swapping,

where two remote particles can become entangled through interactions of particles with which they were each previously entangled [16]. An example of an entanglement swapping scheme is shown in Fig. 2.5 with a trapped ion source at locations A and B. Each ion is entangled with a photon using one of the schemes described above, with the polarization entanglement scheme being shown. The photons are coupled into single mode fibers and routed to a Bell state measurement setup, consisting of a 50/50 beam splitter and two photodetectors. The two photons have a probability to take different paths, and upon doing so, they interfere and cause both detectors to note an event simultaneously. The coincident detection event annihilates the two photons and leaves the remote ions entangled. This heralded entanglement scheme has been demonstrated in a laboratory setting using two Yb ions in separate vacuum chambers separated by several meters [17] [18].

Although quantum repeaters solve the issue of loss of photons during transmission, they are inefficient for ions that operate in the UV or visible spectrum. Quantum repeaters would need to be spaced at sub-kilometer intervals, which is technically and economically infeasible. Thus, to be effective in a practical sense, the photons would need to be in the telecommunications range where quantum repeater spacing could be in the 10's to 100's of kilometers. To date there exists no good quantum memory system that operates in the 1310 nm or 1550 nm bands.

An alternative approach using quantum repeaters based on trapped ions is to down-convert the frequency of the photon before sending it through the communication fiber. There exist several methods to convert the frequency of light, but care must be taken to ensure that the system does not decohere and that minimal noise is introduced. Wave mixing in nonlinear optics has been shown to fill these goals [19] [20], and can provide complete conversion if proper conditions are filled.

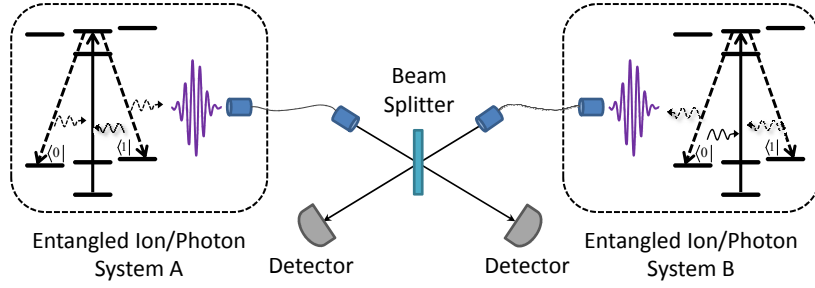


FIGURE 2.5: A quantum repeater scheme using trapped ions, with entanglement swapping to allow long distance quantum communication [17].

2.2 Difference frequency mixing in nonlinear crystalline materials

In a typical linear medium, an applied electric field causes motion of the electrons about their nucleus at the frequency of the incident electric field [21]. This is referred to as the polarizability of the material, and it is related to the applied electric field by

$$\vec{P}(t) = \epsilon_0 \chi \vec{E}(t) \quad (2.1)$$

where ϵ_0 is the permittivity of free space and χ is the linear susceptibility of the material. In nonlinear materials, the electron displacement is not linearly related to the incident electric field. For nonlinear materials, the polarization can be written as a power series [21]

$$\vec{P}(t) = \epsilon_0 \chi \vec{E}(t) + \epsilon_0 \chi^2 \vec{E}(t)^2 + \epsilon_0 \chi^3 \vec{E}(t)^3 \dots \quad (2.2)$$

showing both the linear part of the polarizability, $\epsilon_0 \chi \vec{E}(t)$, and the higher order terms. The higher order terms in Eq. (2.2) give rise to numerous nonlinear wave mixing effects, from harmonic generation to sum and difference frequency generation. In the processes of interest, only the second order susceptibility is important, but the derivations that follow are similar for higher order terms. Materials that have a high

degree of anisotropy have a very large second order susceptibility due to direction dependent forces acting on the electrons.

The second order polarizability can be written as

$$\vec{P}_{NL}^{(2)}(t) = \epsilon_0 \chi^2 \vec{E}(t)^2 \quad (2.3)$$

or in the frequency domain

$$\vec{P}_i(\omega) = \epsilon_0 \sum_{j,k} \sum_{n,m} \chi_{ijk}^2 E_j^{\omega_n} E_k^{\omega_m} = 2\epsilon_0 \sum_l \sum_{n,m} d_{il} E_j^{\omega_n} E_k^{\omega_m} \quad (2.4)$$

where the use of the Kleinmann symmetry [22] allows the substitution of $d_{il} = \frac{1}{2}\chi_{ijk}^{(2)}$, reducing the rank three tensor to a simpler rank 2 tensor. The d parameter is known as the nonlinear coefficient, and it gives the strength of the induced polarization relative to the input field polarization (which is a material dependent property).

In the difference frequency generation process, the mixing of input fields results in an induced polarization equal to the difference of the input frequencies. This induced polarization in each coordinate direction as a function of input polarization is given by

$$\begin{pmatrix} \tilde{P}_x^{\omega_1-\omega_2} \\ \tilde{P}_y^{\omega_1-\omega_2} \\ \tilde{P}_z^{\omega_1-\omega_2} \end{pmatrix} = 4\epsilon_0 \begin{pmatrix} d_{11} & d_{12} & d_{13} & d_{14} & d_{15} & d_{16} \\ d_{21} & d_{22} & d_{23} & d_{24} & d_{25} & d_{26} \\ d_{31} & d_{32} & d_{33} & d_{34} & d_{35} & d_{36} \end{pmatrix} \begin{pmatrix} \tilde{E}_x^{\omega_1} \tilde{E}_x^{\omega_2} \\ \tilde{E}_y^{\omega_1} \tilde{E}_y^{\omega_2} \\ \tilde{E}_z^{\omega_1} \tilde{E}_z^{\omega_2} \\ \tilde{E}_y^{\omega_1} \tilde{E}_z^{\omega_2} - \tilde{E}_z^{\omega_1} \tilde{E}_y^{\omega_2} \\ \tilde{E}_x^{\omega_1} \tilde{E}_z^{\omega_2} - \tilde{E}_z^{\omega_1} \tilde{E}_x^{\omega_2} \\ \tilde{E}_x^{\omega_1} \tilde{E}_y^{\omega_2} - \tilde{E}_y^{\omega_1} \tilde{E}_x^{\omega_2} \end{pmatrix} \quad (2.5)$$

showing that the choice of incident electric field polarizations affects not only the axis of induced polarization, but also the nonlinear coefficient that couples them. As will be shown in later sections, the choice of nonlinear coefficient plays a vital role in achieving efficient frequency conversion.

Derivation of the equation that govern the generation of the difference frequency wave begins with the nonlinear wave equation

$$\nabla^2 \tilde{E}_i - \frac{n_i^2}{c^2} \partial_t^2 \tilde{E}_i = \frac{1}{n_i^2 c^2} \partial_t^2 \tilde{P}_n^{\text{NL}} \quad (2.6)$$

Focusing only on 2nd order processes (i.e. three wave mixing), there will be three fields present with frequencies of the pump (the highest frequency input $\tilde{E}_p(z, t) = A_p e^{i(k_p z - \omega_p t)} + c.c.$), signal (the lowest frequency input $\tilde{E}_s(z, t) = A_s e^{i(k_s z - \omega_s t)} + c.c.$), and idler (the generated wave $\tilde{E}_i(z, t) = A_i e^{i(k_i z - \omega_i t)} + c.c.$). The wave vector, k is given by

$$k_x = \frac{n_x \omega_x}{c} = \frac{2\pi n_x}{\lambda_x} \quad (2.7)$$

with the dependence of the index of refraction, n , on the frequency of the wave denoted by the respective subscript. The induced polarization will depend on the pump and signal input fields as described in Eq. (2.5)

$$\tilde{P}_i = 4\epsilon_0 d A_p A_s e^{i((k_p - k_s)z - \omega_i t)} \quad (2.8)$$

for the case of incident waves having the same polarization direction.

Putting Eq. (2.8) and the input fields into Eq. (2.6) gives the equation for the generated idler field (neglecting absorption, using the non-depleted pump approximation, and assuming plane waves).

$$\frac{dA_i}{dz} = -i \frac{2id\omega_i}{c^2 k_i} A_p A_s e^{i\Delta k z} \quad (2.9)$$

$$\Delta k = k_p - k_s - k_i \quad (2.10)$$

For the case of focused Gaussian beams and no pump depletion, the generated idler power is found to be [23] [24] [25]

$$P_i = P_p P_s \frac{32\pi^2 d_{eff}^2 l}{\epsilon_0 c n_{idler} \lambda_i (n_s \lambda_p + n_p \lambda_s)} h(\xi, \sigma, \mu, \alpha, l) \text{Sinc}^2\left[\frac{\Delta k l}{2}\right] \quad (2.11)$$

The Gaussian reduction factor term, $h(\xi, \sigma, \mu, \alpha, l)$, in Eq. (2.11) takes into account the focusing of the gaussian beams and any walkoff that may be experienced [26]. For the case of colinear propogating waves with their focus at the center of the crystal and negligible absorption, the maximum value of $h(\xi, \sigma, \mu, \alpha, l)$ is found to be 1.064 [26]. The length of the crystal is denoted by l . From this formula, it is apparent that for high conversion, a large nonlinear coefficient is desired as is a long crystal length and high pump power.

The $\text{Sinc}^2[\frac{\Delta k L}{2}]$ portion of the generated power determines the bandwidths of the mixing process, as it is maximized for $\Delta k = 0$. Δk is a measure of the phase mismatch of the waves, and can be written as

$$k_{pump} - k_{signal} - k_{idler} = \frac{2\pi n_{pump}}{\lambda_{pump}} - \frac{2\pi n_{signal}}{\lambda_{signal}} - \frac{2\pi n_{idler}}{\lambda_{idler}} \quad (2.12)$$

The index of refraction for most materials is a strong function of temperature, frequency, and polarization angle for birefringent materials. In dispersive media, perfect phase matching ($\Delta k = 0$) is achieved by angle tuning the input beams, critical phase matching, or by temperature tuning the crystal, non-critical phase matching. Both of these processes are limited in the frequency conversions they allow. Additionally, critical phase matching suffers from beam walk-off causing a reduced interaction length and beam distortion.

An alternative method of phase matching involves periodically reversing the dipole moment (the d coefficient) of the crystal every time the phase mismatch amounts to $\frac{\pi}{2}$ or an odd multiple thereof. This process is called quasi-phase matching (QPM), and it alters equation (2.12) to a new form that includes a crystal momentum k_Λ

$$k_{pump} - k_{signal} - k_{idler} - k_\Lambda = \frac{2\pi n_{pump}}{\lambda_{pump}} - \frac{2\pi n_{signal}}{\lambda_{signal}} - \frac{2\pi n_{idler}}{\lambda_{idler}} - \frac{2\pi m}{\Lambda} \quad (2.13)$$

Λ is the poling period of the crystal and m is the order of poling used. If it is assumed that the poling is rectangular in nature, meaning that it can only alternate between having a $+d$ or $-d$ value, the new effective nonlinear coefficient is found to be [21]

$$d_{eff} = \frac{2}{m\pi} \text{Sin}\left(\frac{m\pi}{2}\right) \quad (2.14)$$

which shows that only odd higher order poling periods are allowed and they reduce the nonlinear coefficient by a factor of m .

Although the DFG scheme has been detailed, for it to be useful for quantum communication, the conversion process must not cause decoherence of the input photon. Proof that frequency conversion conserves the photon's information has been performed [27], [28] [29], which demonstrated that an entangled photon pair retains their entanglement once one of the photons is translated in frequency. No experiment to date has converted from the UV to the IR, which limits their usefulness to certain atomic species. Some of the above experiments also suffer from excess noise generated in the nonlinear crystal, causing a degradation in the communication fidelity.

2.3 Raman scattering and parametric fluorescence noise in crystalline media

As part of a communication channel, the conversion process not only needs to have a high throughput, but it also needs to contribute as little noise as possible to the system. There are several sources where noise can occur that are intrinsic to the experiment, as shown in Fig. 2.6. These are parametric downconversion, Stokes scattering, and anti-Stokes scattering. Parametric downconversion (PDC) is a multi-photon process where a high energy photon decays into two or more lower energy photons. If the PDC noise overlaps the signal or idler, the noise can not be filtered. Stokes scattering involves the release of energy in the form of a lattice vibration

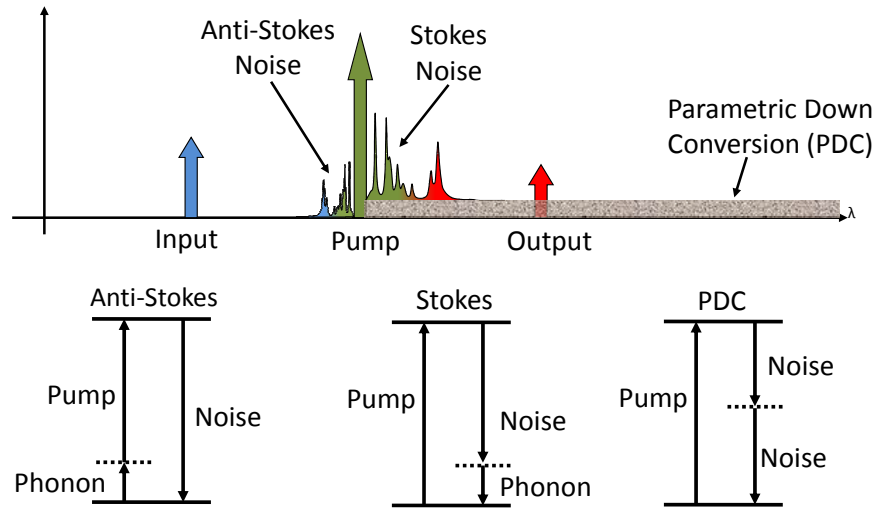


FIGURE 2.6: The strong pump light needed for high efficiency frequency conversion undergoes several processes that alter its frequency and introduce noise on the output. Parametric downconversion is a three photon process where a high energy photon decays into two lower energy photons. Stokes scattering involves the emission of a phonon into the crystalline material, resulting in a lower frequency photon. Anti-Stokes scattering is the reverse process with a phonon being absorbed by the photon leading to a higher frequency photon being created. An output signal longer in wavelength than the pump is accompanied by excessive noise.

(phonon). This loss of energy results in a photon with a lower frequency than the input. Anti-Stokes scattering is the reverse process, whereby a phonon is absorbed from the media creating a photon with a higher frequency. Of these three processes, the most severe is the parametric fluorescence due to its very broadband nature and high probability of occurring. By keeping all signals of interest at a higher frequency than the strongest laser source, both parametric fluorescence and Stokes scattering noise can be avoided, leaving only anti-Stokes noise.

The background provided in this chapter serves as the basis for the UV to NIR frequency conversion experiment. Through proper experiment design, high conversion efficiency should be realizable with minimal noise added. The next few chapters detail the experimental setup and give an analysis of the conversion efficiency of 369.5

nm to 708 nm with limited laser power. Anti-Stokes noise is determined as a function of experimental parameters, and methods to reduce its affect on the communication channel are given. An investigation of the limitations of the setup as designed will then be discussed as it pertains to a trapped Yb ion quantum repeater.

Experimental Overview of multi-stage UV to NIR quantum frequency converter

A low noise method of connecting the 369.5 nm transitions of ytterbium ions to the telecom wavelength of 1310nm requires multiple difference frequency generation stages to avoid the parametric downconversion noise as describe in Sec. 2.3, with the high power pump in each section needing to be longer in wavelength (lower in energy) than either the signal or the output. Note that the definition of pump, idler, and signal have been changed from the previous chapter. The pump now refers to the high power input, the signal refers to the input that carries the information, and the idler or output is the converted signal. In the previous section, the pump referred to the high energy input, while it is more convenient for it to denote the high power input. A single stage conversion process would dictate a pump wavelength of 514.7 nm, much higher in energy than the output signal allowing PDC noise to overlap the output. If no constraints are given on the number of pump sources, then the conversion can happen in two stages, where the first stage converts the 369.5 nm signal from the ion to an intermediate signal and a second stage performs the final

conversion to 1310 nm. For simplicity, a single pump source can be used throughout each step, which would entail three stages with a pump frequency of 1544.1 nm which is three times the wavelength of a single stage. The signal is converted to 485.7 nm in the first stage, then to 708.6 nm in the second, and to 1310 nm in the final stage.

Although a three stage process would accomplish the conversion, a reduction can be made if another frequency conversion process is used. The first two stages can be combined if a pump of twice the energy is used, which can be done by using the second harmonic of the original 1544 nm pump. Although the same amount of frequency conversion stages are needed (3), benefits are gained because the difference frequency mixing process has much more stringent requirements on the experimental parameters.

Using this architecture, a two-stage conversion process has been designed where the pump of the first stage is generated via second harmonic of the pump for the second stage, as shown in Fig. 3.1. A 1544 nm pump serves as the single external laser needed by the system, and a portion of it is converted to 772 nm. This 772 nm signal is used as a pump with the initial 369.5 nm signal from the ion in a DFG process to generate a 708.6 nm intermediate wavelength. This intermediate signal is then combined with the residual 1544 nm pump to create the final output at 1310 nm. In each stage, the pump is sufficiently far from the output signal so that optical filtering can be used to reduce noise counts. This thesis details only the first difference frequency generation stage and the second harmonic generation (the dashed box in Fig. 3.1). Other groups have already converted from the 710 nm to 1310 nm wavelength regime [27], so the primary interest is in transferring the signal out of the UV because that is a much harder wavelength to work with due to the high loss it suffers in most materials.

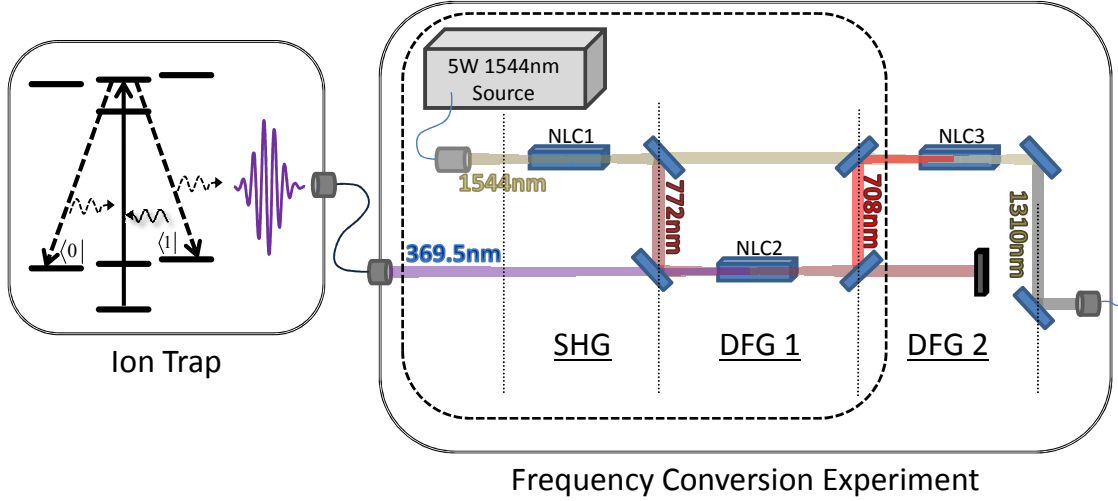


FIGURE 3.1: Light output from a ytterbium ion trap is transferred to the frequency conversion experiment by a short optical fiber. The pump for the first DFG stage is created through SHG using a PPLN crystal (NLC1), and then fed to a second PPLN crystal (NLC2) which converts the 369.5 nm signal from the ion to the intermediate frequency of 708 nm. The last stage will convert this frequency to the final desired 1310 nm telecom band. This thesis focuses only on the processes in the dashed box.

3.1 772nm pump creation via second harmonic generation

The concept of second harmonic generation (SHG) can be understood from the theory presented in Sec. 2.2 if the case of degenerate sum frequency generation is considered. Rather than allowing two separate waves to interact to create a third, a single input wave interacts with itself creating a polarization in the material that transforms Eq. (2.4) into [22]

$$\begin{pmatrix} \tilde{P}_x^{2\omega} \\ \tilde{P}_y^{2\omega} \\ \tilde{P}_z^{2\omega} \end{pmatrix} = 2\epsilon_o \begin{pmatrix} d_{11} & d_{12} & d_{13} & d_{14} & d_{15} & d_{16} \\ d_{21} & d_{22} & d_{23} & d_{24} & d_{25} & d_{26} \\ d_{31} & d_{32} & d_{33} & d_{34} & d_{35} & d_{36} \end{pmatrix} \begin{pmatrix} (\tilde{E}_x^\omega)^2 \\ (\tilde{E}_y^\omega)^2 \\ (\tilde{E}_z^\omega)^2 \\ 2\tilde{E}_y^\omega \tilde{E}_z^\omega \\ 2\tilde{E}_x^\omega \tilde{E}_z^\omega \\ 2\tilde{E}_x^\omega \tilde{E}_y^\omega \end{pmatrix} \quad (3.1)$$

Following the same process as the DFG derivation, the second harmonic conver-

sion efficiency can be found as [30] [22]:

$$\eta_{shg} = \frac{P_{sh}}{P_{ff}} = \text{Tanh} \left(\sqrt{\frac{16\pi^2 d_{eff}^2}{\epsilon_0 c \lambda_{ff}^3 n_{ff} n_{sh}}} P_{ff}^2 l h \right)^2 P_{ff} \text{Sinc} \left(\frac{\Delta k l}{2} \right)^2 \quad (3.2)$$

taking into account depletion of the pump and the Gaussian reduction factor (h) due to focusing of the beams. The same Sinc^2 dependence on phase matching is found as with the DFG case. Subscripts refer to the fundamental frequency (ff) or to the second harmonic (sh). The variables that have the largest effect on the conversion are the crystal length (l), the pump power (P_w), and most importantly, the nonlinear coefficient (d_{eff}) which has a squared dependence.

In choosing a crystal for SHG, the range of transparency, the nonlinear coefficient, and the ability to achieve phase matching all play a vital role. Lithium niobate is a uniaxial crystal that is transparent from 330 nm to several microns and has a high d_{33} nonlinear coefficient. In addition, lithium niobate can also be poled using high electric fields and patterned electrodes allowing QPM [31]. To use the d_{33} coefficient, as can be seen from Eq. (3.1), the input needs to be polarized along the z-axis resulting in an induced polarization along the z-axis.

To fulfill the QPM condition, the poling period of the crystal needs to be determined via the modified form of Eq. (2.13) for SHG

$$k_{\lambda/2} - k_{\lambda} - k_{\lambda} - k_{\Lambda} = \frac{2\pi n_{\lambda/2}}{\frac{\lambda}{2}} - \frac{4\pi n_{\lambda}}{\lambda} - \frac{2\pi m}{\Lambda} = 0 \quad (3.3)$$

with the index of refraction given by the temperature and wavelength dependent Sellmeier equation [32]. The choice of temperature, although somewhat arbitrary, does play a role in reducing photorefractive damage that can occur in lithium niobate when high intensity light is used. To reduce the photorefractive effect, the crystals are run at higher temperatures and they are also doped with magnesium oxide. For this experiment, a temperature of around 70° was used resulting in a poling

period of roughly $19.1 \mu\text{m}$ for the 1544 nm to 772 nm conversion. A 4 cm long periodically poled lithium niobate (PPLN) crystal was used with 5 different poling periods centered around $19.1 \mu\text{m}$ to allow tuning if needed. The facets were AR coated to reduce reflections from the input and output facet to less than 0.5% at both the 1544 nm fundamental frequency and the 772 nm second harmonic.

The experimental layout is shown in Fig. 3.2. The primary laser source is a very low noise RIO Planex 1544 nm DFB laser with a polarization maintaining fiber pigtail, which feeds a IPG ytterbium doped fiber amplifier (EDFA) that provides an amplified output of up to 5 W . The output of the EDFA feeds a collimator, with the polarization preserved as the frequency conversion process is dependent on the polarization. Collimated 1544 nm output from the EDFA is fed through a focusing lens and aligned to the crystal via a three-axis mirror. The spot size was chosen to allow maximum conversion efficiency [26] while not clipping the beam. The crystal itself sits on a three-axis stage for alignment purposes as the aperture is only $500 \mu\text{m}$ by $500 \mu\text{m}$. For temperature stabilization, the crystal is located in an oven and controlled with a Wavelength Electronics temperature controller providing fluctuations less than 0.01°C . A lens is placed on the output of the crystal that recollimates the light, followed by a dispersing prism that separates the 1544 nm light from the 772 nm light. A pick-off mirror dumps the 1544 nm light until it is needed for the second DFG stage.

3.1.1 SHG Results

Verification of the beam overlap and poling quality of the PPLN crystal can be gained by measurement of the converted power as a function of temperature or pump wavelength. Both mechanisms provide similar results in that they affect the phase matching condition, giving the Sinc^2 behavior described previously. To test the temperature tuning bandwidth, the pump wavelength and pump power was held

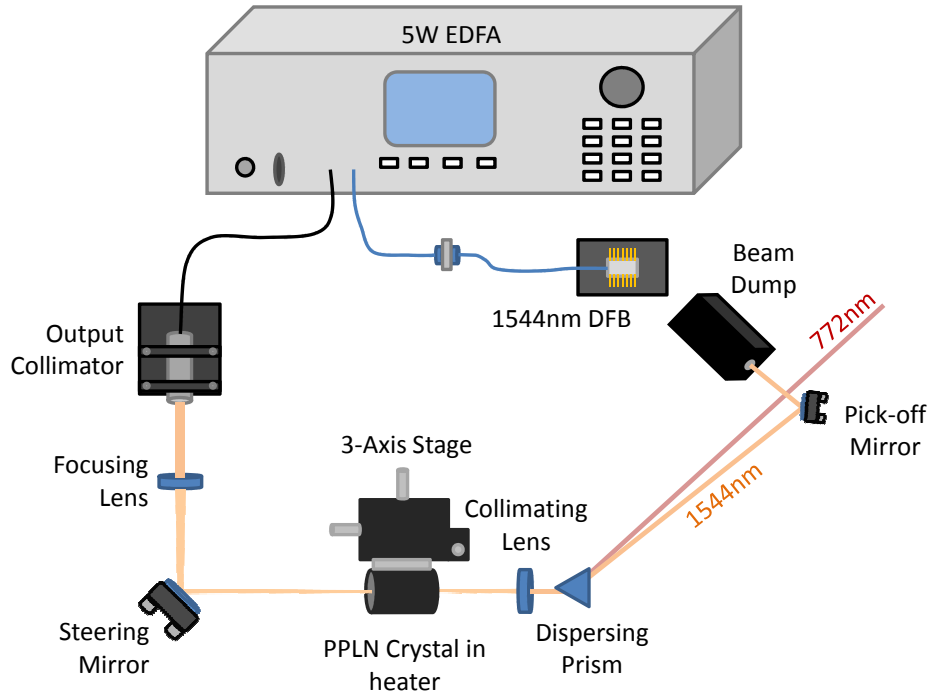


FIGURE 3.2: To generate the 772 nm light needed for the DFG stage, a 1544 nm seed laser feeds a 5W EDFA that will be partially converted via SHG. The collimated output from the EDFA gets focused by a lens gets aligned to the crystal via a tilt mirror. The crystal is located in an oven for temperature stabilization with a 3-axis stage for precise control over the waist position. The fundamental and second harmonic are collimated on the output and separated by a dispersing prism. The 1544 nm beam is dumped until needed for future stages.

constant as I swept the temperature of the crystal, with the output power being measured at 0.1°C intervals. My result are shown in Fig. 3.3, which verifies that my experimental data (red dots) corresponds well with the theoretical curve (blue line).

Knowing the temperature tuning curve allows the QPM condition to be found, which corresponds to the peak of the plot in Fig. 3.3. With the temperature fixed to this value and the seed laser held to a constant frequency, the conversion efficiency can be determined by varying the power of the 1544 nm pump signal, as shown in Fig. 3.4. Using a first order poling period reduces the nonlinear coefficient by a

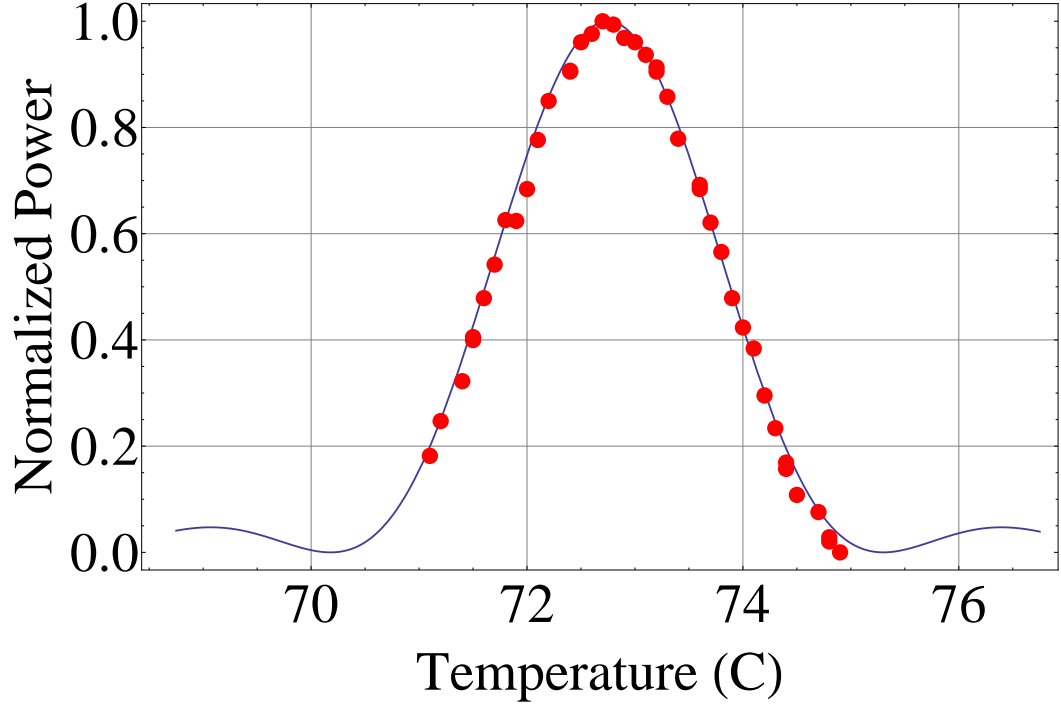


FIGURE 3.3: The temperature tuning curve of the second harmonic generation stage. As the temperature of the crystal is varied, the output power changes due to changes in the phase matching condition. For maximum conversion, the crystal should be held at the temperature corresponding to the peak (around 72.6°C).

factor of $2/\pi$ as determined by Eq. 2.14. Values of the d_{33} coefficient vary depending on the wavelength, with literature values ranging from 20.3 pm/V at 1313 nm to 20.3 pm/V at 852 nm [33]. The theoretical (blue) curve is given by solving for P_{sh} in Eq. 3.2 with $d_{eff} = \frac{2}{\pi} \times 20.3\text{pm/V}$, $\Delta k = 0$, and refractive indices from the Sellmeier equation [32]. Red dots denote my collected experimental data, and the dashed orange curve is a fit to the experimental data. My experimental SHG process is approximately 90% of the theoretical. This discrepancy can be due to a number of issues, including using a theoretical nonlinear coefficient at a shorter wavelength, potential duty cycle errors during the periodic poling of the crystal [34], or nonideal beam alignment. The overall result is a maximum power output of 393 mW at 772 nm with a maximum input power of 5 W from the EDFA.

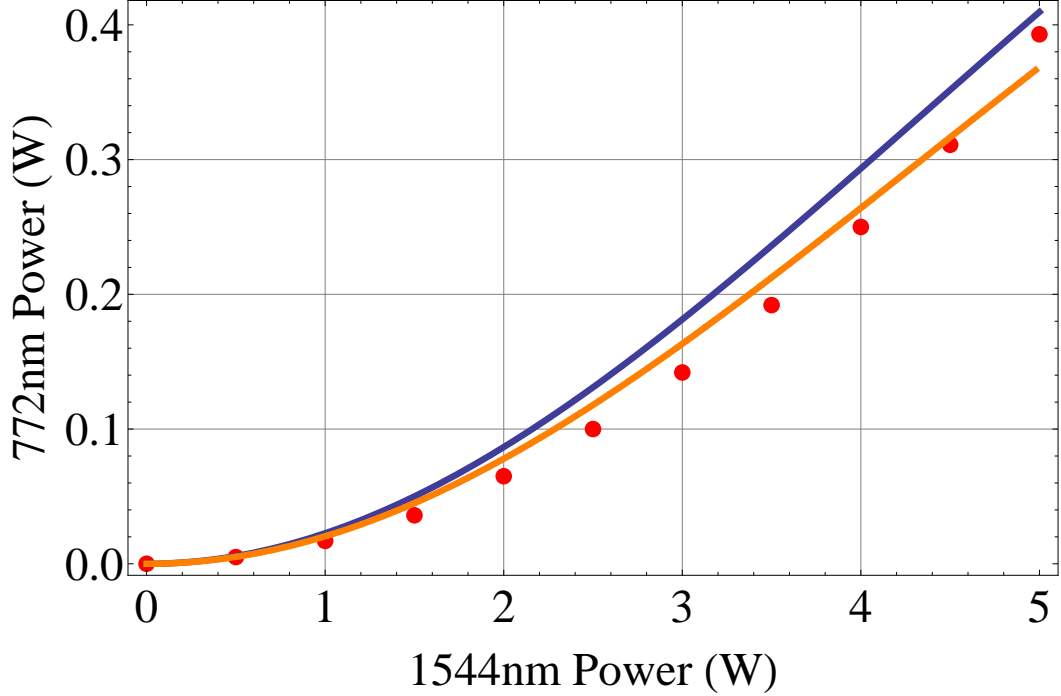


FIGURE 3.4: Generated 772 nm power is plotted as a function of 1544 nm input power. The blue curve represents the theoretical conversion value with $\Delta k = 0$ and $d_{eff} = \frac{2}{\pi} \times 20.3\text{pm/V}$. Red dots denote my experimentally collected values with the orange dashed curve fit to them. My experiment achieved 90% of the ideal expectation.

3.2 Difference Frequency Generation of 708 nm Intermediate Frequency

With the creation of a high power 772 nm source, attention can turn to the DFG stage that eventually converts the 369.5 nm signal from the ion to a 708 nm output. Throughout this section, the definitions of the pump, signal, and idler are altered slightly from those given in Section 2.2. In a typical DFG process, the pump is the highest energy input photon, the signal is the other input photon, and the idler is the generated output photon. With the current scheme, however, the highest energy input is the 369.5 nm signal from the ion and the 772 nm light generated from the SHG stage has the highest power. Thus, for the rest of the thesis, the 369.5 nm light

will be referred to as the signal, the 772 nm light as the pump, and the 708 nm signal as the idler or output. The derivation given in Section 2.2 still hold with the correct substitution of terms made.

As with the second harmonic generation stage, a crystal is needed that can fulfill the difference frequency phase matching condition, has minimal loss, and has a high nonlinear coefficient. Several crystals were researched from lithium tantalate (smaller nonlinear coefficient) to potassium titanyl phosphate (high absorption in the UV), with PPLN remaining as the best choice. The QPM condition for this process is given by

$$k_{signal} - k_{pump} - k_{idler} - k_{\Lambda} = \frac{2\pi n_{369.5nm}}{369.5nm} - \frac{2\pi n_{772nm}}{772nm} - \frac{2\pi n_{708nm}}{708nm} - \frac{2\pi m}{\Lambda} \quad (3.4)$$

resulting in a first order ($m = 1$) poling period of 1.94 μm . This poling period length is far below the commercially available poling period range, since at such small distances the domains start to merge resulting in a poor quality crystal. Therefore, a third order poling period is used, reducing d_{eff} by a third (from Eq. (2.14)). Power is reduced by a factor of 9 since it is dependent on d_{eff}^2 . As will be seen, this limitation plays a huge role in reduced conversion efficiency and increased noise.

Initial experiments used a custom PPLN crystal designed to operate at 100°C with a periodicity of 5.73 μm , but the crystal was found to be unsuitable due to the large defects created during the poling process. To reduce cost, an off-the-shelf PPLN crystal was desired as a replacement, but only limited periodicities were available. A period of 5.29 μm was chosen (originally for first order SHG of 986 nm light), requiring an operating temperature of 283°C. Due to the highly dispersive nature of lithium niobate in the ultraviolet regime, small changes in temperature result in large changes in Δk , leading to very narrow tuning bandwidths. A custom oven was built to house the PPLN crystal along with a Cryocon temperature controller which has shown stabilities down to 0.005°C. The facets of the crystal were not AR coated,

so losses due to Fresnel reflections were suffered.

The DFG layout is shown in Fig. 3.5 using a frequency stabilized diode laser as a 369.5 nm UV source for testing rather than the signal from a Yb ion. The fiber coupled output of the UV laser is routed through polarization paddles to control the polarization then to a collimator. An adjustable telescope provides beam transformation to get the ideal spot size for high conversion ($w_0 \approx 19\mu\text{m}$) with tilt and translate mirrors providing the degrees of freedom needed for proper beam overlap with the 772 nm pump. The 772 nm light goes through a similar adjustable telescope and alignment mirror stage. Both beams are focused with lenses before being combined with a dichroic beam combiner. The crystal itself is mounted in the custom heater on a three axis stage that also allows rotation about two axes. To separate the generated 708 nm signal from the strong pump and unconverted 369.5 nm signal, two Semrock fluorescence filters are used which have a bandpass of 40 nm centered at 710 nm and a bandpass of 57 nm at a center of 697 nm providing attenuation of greater than OD15. Measurement of the 708 nm signal is provided by a Newport detector.

3.2.1 DFG Results

As with the SHG experiment, the temperature tuning bandwidth provides information about the crystal quality, beam alignment, and system stability. The 772 nm pump power and frequency were held constant, as was the 369.5 nm signal from the diode laser and the temperature was varied, with my results shown in Fig. 3.6. Red dots denote the experimental data I collected, while the solid blue curve is the theoretical tuning curve assuming the inputs are plane waves (i.e. no diffraction). An expanded theory on DFG that takes into account the diffraction of the focused Gaussian beams is given in [35] and plotted with the dashed blue curve, which displays a slightly broader tuning curve with an increased tail at lower temperatures,

corresponding to $\Delta k < 0$. The tail can be understood from the \vec{k} -diagram where any angles of k can project to form a smaller total k vector, but it is impossible to form a larger k vector than with all k at zero angle. Despite this correction, the experimental data is still much broader than the theoretical curve. The dashed orange curve is a fit to the experimental data, corresponding to a 3 times larger bandwidth. The origin of the mismatch between theory and experiment is still undetermined and is currently under investigation.

The most important aspect of the conversion process is the conversion efficiency, because a low conversion would result in a high loss for the communication system. Fig. 3.7 shows the amount of conversion efficiency of 708 nm light as a function of 772 nm power that I achieved. Of importance to note again is the use of a 3rd order poling period that results in a theoretical factor of 9 reduction in the conversion efficiency. The blue curve in Fig. 3.7 denotes the theoretical 708 nm conversion efficiency with the assumption of Fresnel reflections at both facets due to lack of an AR coating. Experimental data is again marked by red dots and fit with the orange dashed curve. The result is a conversion efficiency approximately 70% of the theoretical value with a maximum output power of 21 nW with an input of 11 μ W corresponding to an overall efficiency of 0.2% taking into account all losses. The deviations from the ideal conversion efficiency may be partially accounted for by the use of a non-ideal duty cycle [34] and random missing domain sections. Zygo imaging reveals a duty cycle of around 70/30, similar to what the manufacturer claims, and approximately 1% missing domains. The non-ideal duty cycle would cause a 19% reduction in conversion efficiency and the missing domains another 4%. Any further loss may be due to beam alignment issues. Furthermore, the exact nonlinear coefficient of PPLN is unknown for UV wavelengths and the Kleinmann symmetry reduction is not especially valid in such dispersive operating regime. Thus, the theoretical conversion efficiency shown here may be only approximately valid.

Generation of a 708 nm signal from a 369.5 nm input signal using a high power 772 nm pump has been demonstrated, albeit with fairly low conversion efficiency and broader than expected tuning curves. In theory, higher conversion efficiency could be gained by providing more 772 nm pump power. To achieve this, a bowtie cavity has been designed and constructed that should allow a circulating power of greater than 20 W. Knowing the rate of conversion as a function of pump power, it is now crucial to understand how the 772 nm pump affects the noise of the process due to scattering as discussed in Sec. 2.3. In the end, the overall goal is to demonstrate not only high conversion, but a system that maintains an adequate signal-to-noise ratio so as to be useful in quantum communication.

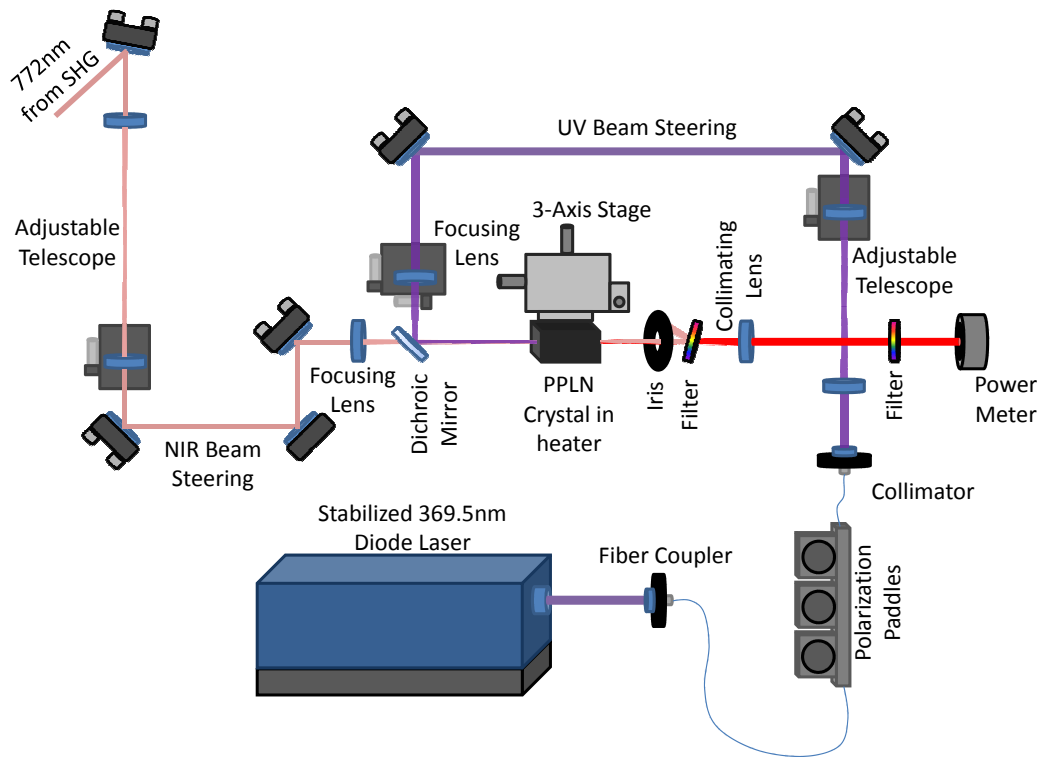


FIGURE 3.5: A frequency stabilized 369.5 nm diode laser is used as a source for DFG testing, and fed to the setup with polarization control provided by fiber paddles. The signal is collimated and transformed via an adjustable telescope and aligned using two steering mirrors. The 772 nm signal from the SHG stage passes through a similar adjustable telescope and steering system (no polarization control is needed since it is fixed from the SHG output). The two beams pass through focusing lenses and are then combined with a dichroic mirror. A three-axis and rotation stage hold the crystal in a custom heater. The output is filtered with two Semrock bandpass filters to provide OD15 attenuation for the residual 772 nm pump and 369.5 nm signal. The generated 708 nm output is measured via a Newport detector.

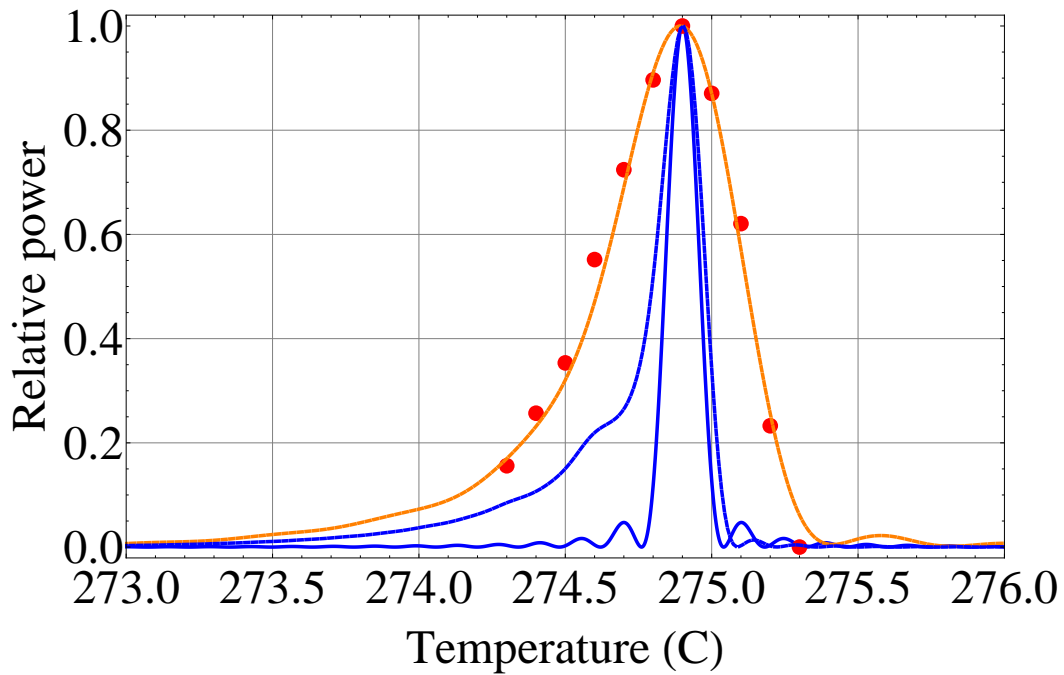


FIGURE 3.6: The quasi-phase matching condition is tested by varying the crystal temperature with the pump power, pump frequency, signal power, and signal frequency held constant. The solid blue curve represents the theoretical tuning behavior assuming plane wave inputs, the dashed blue line is the theoretical with the diffraction of the focused beams accounted for [35], and the red dots denote data from my experiment. The dashed orange curve is a fit to my experimental data showing a 3 times larger bandwidth than predicted.

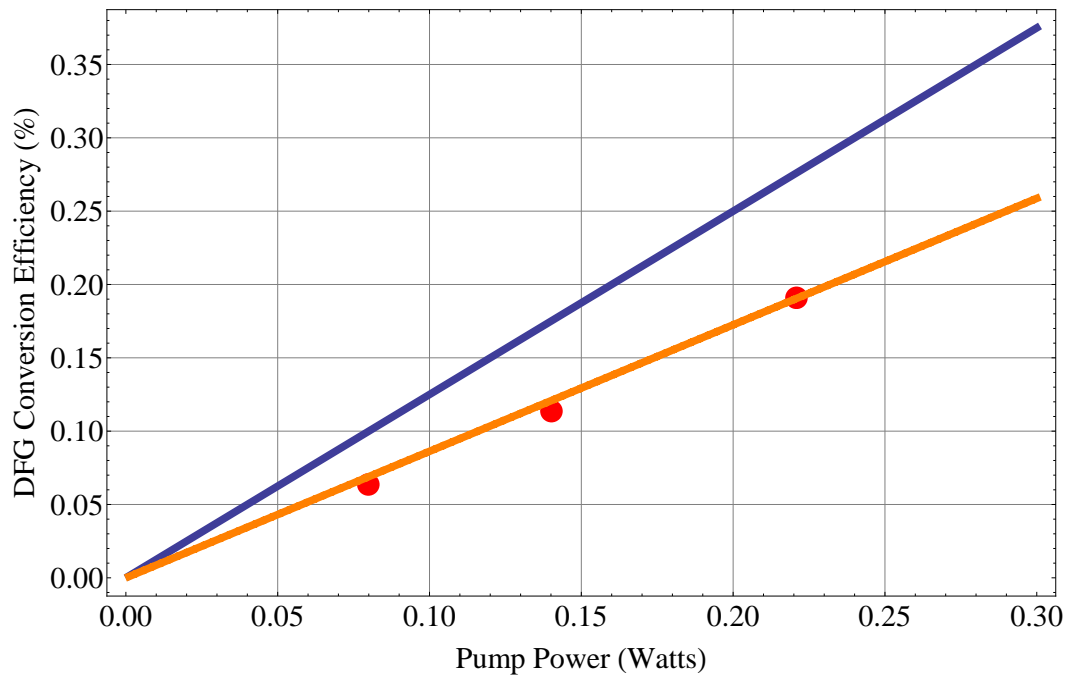


FIGURE 3.7: The conversion efficiency of the DFG between the 369.5 nm signal and 772 nm pump as a function of pump power. The blue line is the theoretical curve based on Eq. 2.11 with a $d_{eff} = 1.8$ pm/V due to 3rd order poling. Experimental data is denoted with red dots and is fit with the dashed orange line. My experiment showed 70% of the conversion efficiency as compared to theory.

Analysis of Raman Scattering Noise in Lithium Niobate

The interaction of light and matter leads to a number of interesting phenomena, not the least of which is the transfer of energy from light to the material (Stokes scattering) and from the material back to light (anti-Stokes scattering). Sec 2.3 detailed why the current downconversion scheme avoids not only the Stokes scattering noise, but also any parametric fluorescence produced by decay of the strong 772 nm pump. Any noise generated in the SHG stage would also occur primarily at wavelengths longer than 1544 nm and suffer poor collection due to the prism and optics, and eventually be filtered out with the bandpass Semrock filters. Thus, the primary noise source is the anti-Stokes scattering that the (SHG generated) 772 nm pump undergoes.

Lithium niobate, a popular material for frequency conversion due to its high nonlinear coefficient, is the material used for the nonlinear crystals in both the SHG and DFG stages. Many analyses of its noise have been performed on the Raman spectrum in bulk form [36] [37] [38], as well as after MgO doping [39] and electric field repoling [40]. The Raman spectrum gives information about the quality of the crystal

with noticeable changes in peak height and width for lithium deficient, congruently grown lithium niobate as well as for crystals operating at higher temperature due to the relaxing of the internal dipole moment.

The Raman spectrum has a dependence on the polarization of the incident and collected light since only vibrational modes that affect or induce a dipole moment will contribute to the scattering process. Lithium niobate has a unit cell with 10 atoms, leading to 30 degrees-of-freedom. The A_2 modes are Raman inactive, and do not contribute to scattering processes. The E modes are active with polarizations in the $\hat{x} - \hat{y}$ plane while the A_1 modes are active with \hat{z} polarization. Of these, 3 are acoustical phonons with very low energy, leaving 4 A_1 , 5 A_2 , and 9 E (doubly degenerate) optical modes [38]. All of the light is \hat{z} polarized in the conversion experiments described previously, so only the noise from scattering with the A_1 modes will be collected.

To verify the quality of our PPLN crystals, the Stokes scattered Raman spectrum was measured using a Horiba Jobin Yvon LabRam ARAMIS Raman microscope. The sample was probed in the \hat{x} direction with a \hat{z} polarization, and the scattered light was collected in the $-\hat{x}$ direction with a \hat{z} polarization ($X(ZZ)\bar{X}$ in spectroscopy terms), a similar setup to the actual DFG experiment only with backward scattered light rather than forward scattered. A pump wavelength of 785 nm was used, providing a close relationship to the actual pump wavelength of 772 nm. Figure 4.1 shows the resulting measurement, with the spectrum agreeing with previous measurements quite well. Only two dominant peaks are easily seen, at 255 cm^{-1} and 633 cm^{-1} , with the peak at 277 cm^{-1} merging into the peak at 255 cm^{-1} and the peak at 322 cm^{-1} too low to be seen.

The Raman microscope only measure the Stokes spectrum, but with the use of the Boltzmann population factor, the Stokes and anti-Stokes scattering intensities at

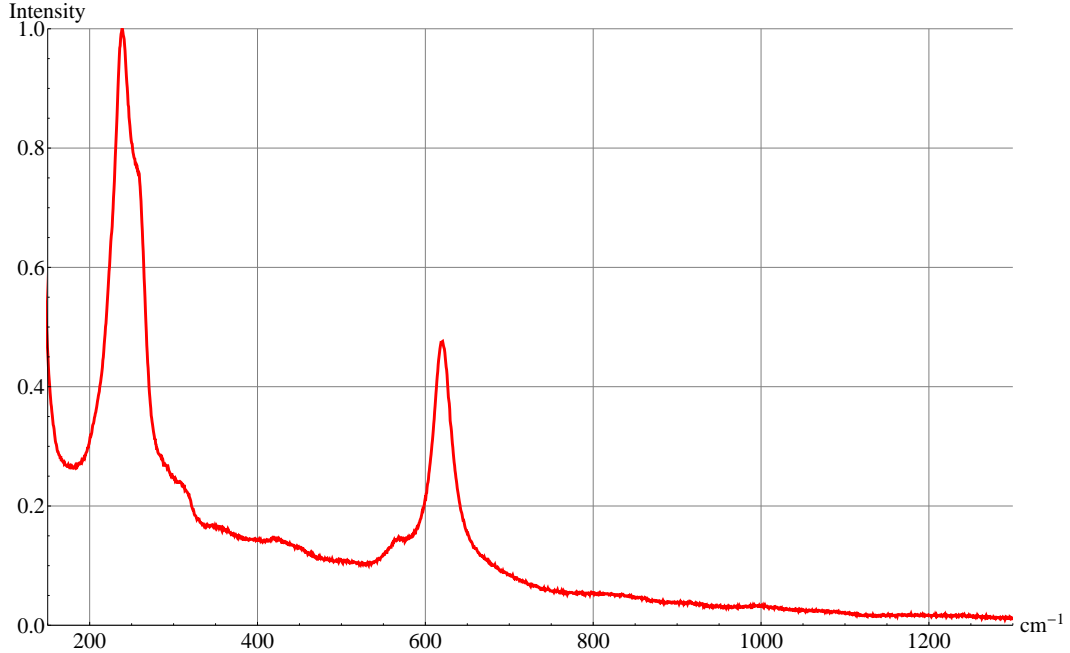


FIGURE 4.1: $X(ZZ)\bar{X}$ Raman spectrum of PPLN crystal with polarizations along the \vec{z} axis, illumination along the \vec{x} axis (the length of the crystal), and backscattered light along the $-\vec{x}$ axis. The four A_1 peaks should be visible, but the first and second are merged together around 255 cm^{-1} and the third is below the noise floor.

equal energy spacings can be related by [5]

$$\frac{I_{AS}}{I_S} = e^{-\frac{h\Delta\nu}{kT}} \quad (4.1)$$

with k denoting Boltzmann's constant, h denoting Planck's constant, T the temperature of the sample, and $\Delta\nu$ the change in frequency from the pump. This exponential relationship demonstrates why noise from anti-Stokes scattering is much more preferable than noise from Stokes scattering. For a given intensity of Stokes scattered noise a distance from the pump, the anti-Stokes intensity at equal but opposite distance would be exponentially smaller. From Eq. (4.1), it can be seen that for the lowest noise, the highest spacing between the pump and signal is required as is operation at the lowest temperature possible. This relationship of low noise to low temperature points to the trade-off made using an off-the-shelf PPLN crystal that operates near

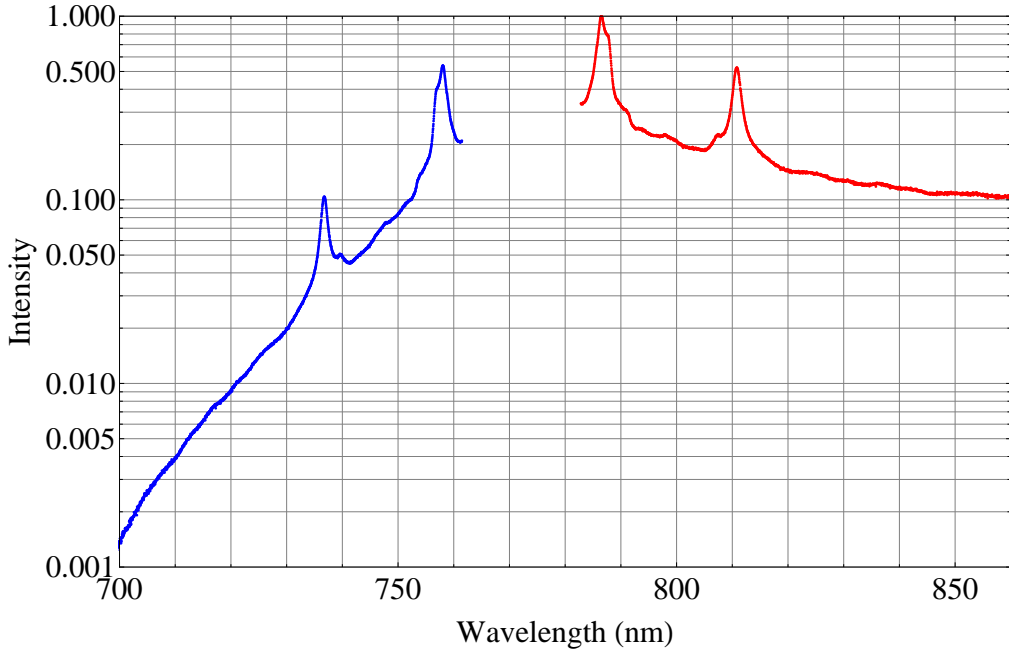


FIGURE 4.2: The normalized Stokes (red) and anti-Stokes (blue) is plotted for a temperature of 283°C . The exponential relationship of the Stoke intensity to anti-Stokes intensity results in a much lower noise photon generation for shorter wavelengths. The DFG signal is at 708 nm, which is far away from the peaks, having the potential for low noise.

283°C . In Fig. 4.2, the normalized Stokes spectrum is plotted (red) along with the converted anti-Stokes spectrum (blue) as a function of wavelength assuming the operating temperature of 283°C and a center wavelength of 772 nm. The output signal at 708 nm is far enough away from the A_1 peaks, and will suffer noise only from the exponential tail. Similar data has been taken for longer wavelength pump, and agrees with the data shown here [5].

With the Stokes and anti-Stokes spectrum analyzed, the actual noise needs to be evaluated as a function of crystal temperature, pump power, and spectral bandwidth. The measurement setup is shown in Fig. 4.3. The 772 nm pump is fed through the crystal in the \vec{x} direction and polarized along the \vec{z} direction. The output light is chopped with a 30 slit optical chopper for use with the lock-in amplifier and passed

through a Semrock filter to attenuate the pump. After attenuation, the light is magnified with a telescope and alignment mirrors and then fed into a monochromator. The monochromator has an adjustable input and output slit to resolve down to 0.2nm with a 1200 lp/mm grating. Dispersion caused by the grating allows different parts of the spectrum to be measured. Detecting the light is done with a Hamamatsu photomultiplier tube using a transimpedance amplifier for gain. This is connected to a Stanford Research Systems digital lock-in amplifier which allows sub-dark noise detection. Calibration of the system was performed using a Newport power meter head to detect the pump signal after attenuation which allows a known power value to correspond to a known voltage value on the lock-in.

The crystal temperature, pump power, and bandwidth were all varied at three different center wavelengths, 710 nm, 720 nm, and 730 nm. The data at 730 nm is not accurate in magnitude since it lies on the edge of passband for the Semrock filter. Thus, the measured value should not be trusted, only the dependence on the variables. My results for all three center wavelengths is shown graphically in Fig. 4.4 with data taken at 710 nm shown in blue, data taken at 720 nm shown in red, and data take at 730 nm shown in green. I found the temperature dependence to follow the expected exponential behavior given in Eq. (4.1), while the power and bandwidth dependence were found to be linear. The noise is given in counts/sec/GHz, meaning that if a certain bandwidth filter is used, the actual noise counts can be found by multiplying the chart data by the filter FWHM bandwidth. Ignoring the data at 730 nm for the reasons given above, the further away from the pump in wavelength the detection is taken, the lower the noise.

Results of my noise analysis show that operating the crystal at lower temperatures is preferential due to the exponential dependence of anti-Stokes scattering on temperature. Lower pump powers are also critical for acheiving a low noise conversion process. Although both conversion efficiency and noise are linearly related to

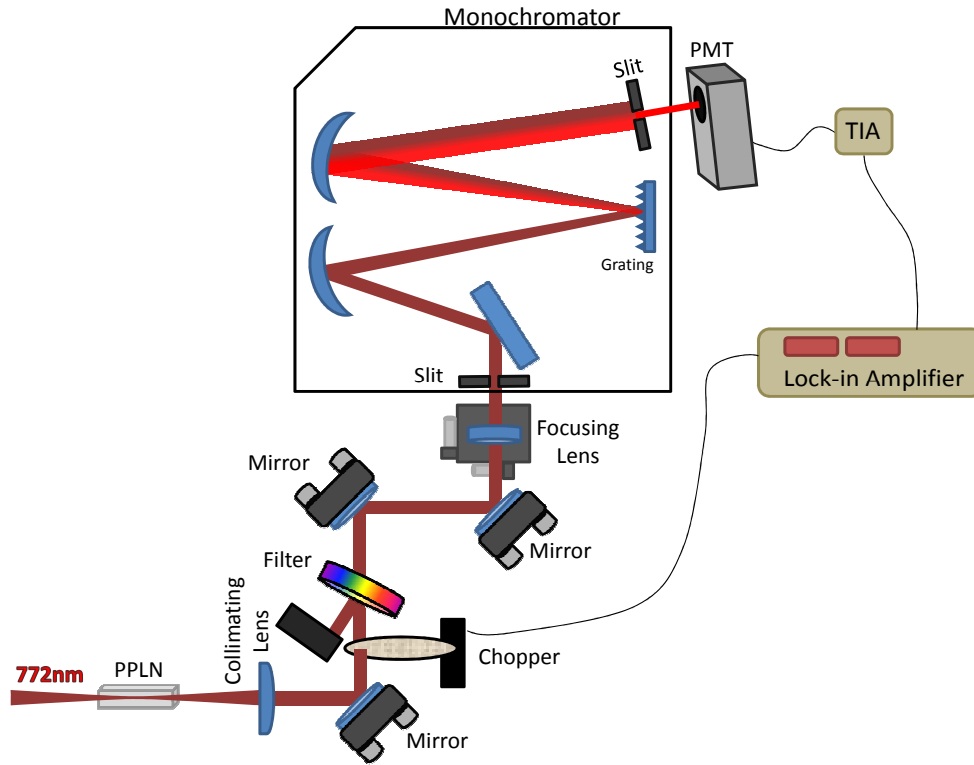


FIGURE 4.3: To measure the anti-Stokes generated noise, the PPLN crystal was pumped with the high power 772 nm light from the SHG stage. The output was collimated and chopped with a 30 slit optical chopper. A Semrock filter attenuates the strong pump and the light is then routed to the monochromator through alignment mirrors and a focusing lens. The input slit, output slit, and grating of the monochromator determine the bandwidth of the measured light. A photomultiplier tube (PMT) detects the light, and its signal is amplified by a transimpedance amplifier (TIA). A lock-in amplifier provides low noise measurement of the signal from the TIA.

pump power, once the pump starts to undergo depletion, the conversion efficiency tapers off. Lastly, the output signal should be filtered as narrowly as possible to reduce noise even further. It would also be advantageous to separate the output wavelength far from the pump. In the DFG experiment described in Chapter 3, the output and pump separation were fixed. The use of a third order poling period has a tremendous negative influence on the noise since a factor of 9 increase in pump

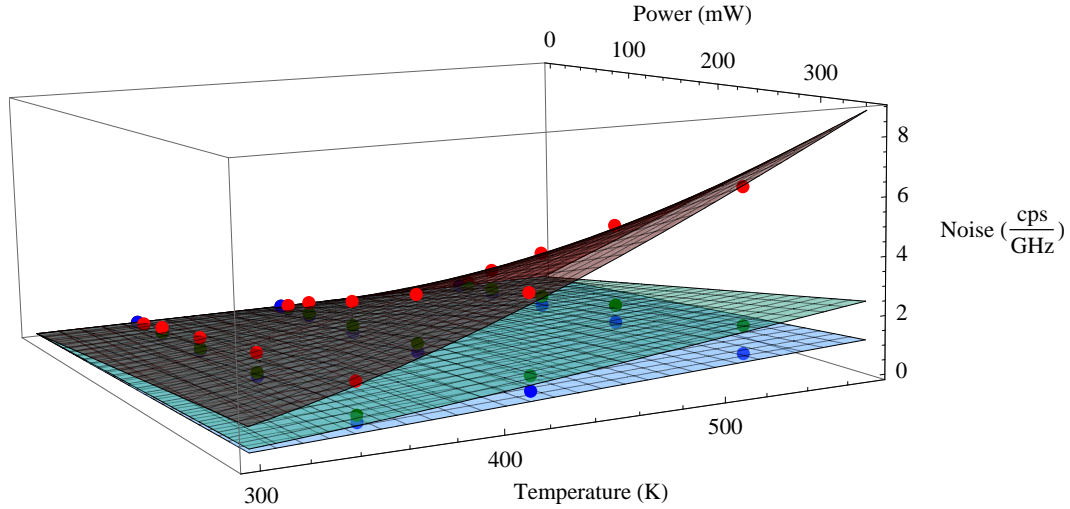


FIGURE 4.4: The measured noise output at 3 different center wavelengths: 710 nm (blue), 720 nm (red), and 730 nm (green) with a pump at 772 nm. The circles represent actual data points I made and the curves are fits. Crystal temperature, pump power, and bandwidth were varied to determine their affect on the noise. The data collected at 730 nm should only be judged for its dependence on the variables given and not on absolute scale since it was partially filtered by the Semrock bandpass filter. Comparing the 710 nm curve to the 720 nm curve clearly shows the noise is reduced at larger separations from the pump wavelength as expected.

power is needed for the same conversion efficiency as a first order poling period. Furthermore, although the off-the-shelf crystal provided savings in time and cost, the disadvantage of having to run at greatly elevated temperatures results in a negative impact on noise. To reduce the noise, then, spectral filtering of the output is needed. Investigation is currently underway to determine the best filtering method to achieve the highest throughput with the lowest noise.

Conclusions

In summary, a scheme to convert the 369.5 nm UV signal from a Yb ion trap has been demonstrated using a long-wavelength pumping scheme to avoid parametric downconversion and Stokes generated noise. A total conversion efficiency taking into account reflections at the crystal facets of 0.20% was achieved. Although this conversion rate is quite low, the ability to send entangled photons over long distances may be a sufficient trade-off. For increased conversion, a buildup cavity has been built that would allow a pump power of up to 30 W, potentially leading to 35% conversion efficiency albeit with an equal increase in noise. Use of long-wavelength pumping has allowed the elimination of parametric downconversion noise as well as Stokes generated noise, which is critical in achieving a high conversion efficiency and low noise quantum frequency conversion setup. With standard fluorescence filtering, a bandwidth of 6.8 nm may be achieved centered at 708 nm. With the maximum single pass pump power of 393 mW and an operating temperature of 283°C, this would correspond to a noise of approximately 3500 cps. Using a buildup cavity with 25 W of circulating 772 nm pump power and a volume holographic grating to get 0.2 nm of filtering, there would be approximately 7,500 cps of noise collected.

In Chap. 2, three different ion/photon entanglement schemes were discussed using either frequency, polarization, or time as the information carrier. The DFG process as described is incompatible with the polarization entanglement scheme since the nonlinear process is polarization dependent and only some of the photons would be converted. Two DFG setups could be used, one to convert each polarization, but the cost and complexity would be vastly increased. The frequency entanglement scheme resulted in photons with a frequency difference of approximately 13 GHz. The 2 cm crystal used in this thesis results in a theoretical phase matching bandwidth FWHM of 15 GHz, but experimental data showed an as yet not understood 3 times broader bandwidth. Thus, the DFG experiment could work with the frequency entanglement scheme but peak conversion could not be obtained for both output frequencies simultaneously. The time-bin entanglement scheme, however, resulted in photons with similar frequency and polarization, only created at different times. Since the DFG process is time preserving, i.e. it would not alter the timing information relative to the two possible output times, it would be ideally suited for this entanglement scheme.

Future experimental directions planned include testing the conversion experiment with the actual output of an ion trap experiment. The collection efficiency of photons from an ion is currently quite low, meaning that if the noise is too high or conversion is too low, the noise will override the signal. As such, the use of a very narrow bandpass volume holographic grating will be evaluated to determine its effect on reducing noise photons collected. As mentioned previously, a buildup cavity has been designed and built in an effort to obtain increased conversion efficiency. To test the buildup cavity, the PPLN crystal would need to be anti-reflection coated. With sufficient conversion efficiency and spectral filtering, it is expected that entanglement preservation can be tested with a Yb ion trap. Ideally, the remote entanglement swapping scheme would be tested over a length of optical fiber to demonstrate the feasibility of an

ion trap quantum repeater, but the square dependence of the photon collection and conversion efficiency may prove to be prohibitively inefficient to the experiment.

An analysis of the a quantum frequency converter relevant to Yb ions has been given. The limitations, such as the use of a third order poling period, proved to have a negative influence on the experiment. The experiment detailed in this thesis shows that if a first order poling period PPLN crystal for the DFG stage were optimized for operation at lower temperatures, a low pump power would be required leading to low noise counts. Even with a third order poling, feasibility of a low noise, high conversion quantum frequency conversion experiment has been shown to be achievable.

Bibliography

- [1] R. L. Rivest et al., “A method for obtaining digital signatures and public key cryptosystems,” *Comm. of the ACM*, vol. 21, no. 2, pp. 120–126, 1978.
- [2] A. Ekert and R. Jozsa, “Quantum computation and shor’s factoring algorithm,” *Rev. Mod. Phys.*, vol. 68, no. 3, pp. 733–753, 1996.
- [3] B. B. Blinov, D. Leibfried, C. Monroe, and D. J. Wineland, “Quantum computing with trapped ion hyperfine qubits,” *Quant. Inf. Processing*, vol. 3, no. 1-5, pp. 45–59, 2004.
- [4] A. T. Pedersen, L. Gruner-Nielsen, and K. Rottwitt, “Measurement and modeling of low-wavelength losses in silica fibers and their impact at communication wavelengths,” *Journal of Lightwave Technology*, vol. 27, pp. 1296–1300, 2009.
- [5] J. S. Pelc, L. Ma, C. R. Phillips, Q. Zhang, C. Langrock, O. Slattery, X. Tang, and M. M. Fejer, “Long-wavelength-pumped upconversion single-photon detector at 1550nm: performance and noise analysis,” *Optics Express*, vol. 19, no. 22, pp. 21445–21456, 2011.
- [6] S. Zaske, A. Lenhard, and C. Becher, “Efficient frequency downconversion at the single photon level from the red spectral range to the telecommunications c-band,” *Optics Express*, vol. 19, no. 13, pp. 12825–12836, 2011.
- [7] T. Wilk, A. Gaëtan, C. Evellin, J. Wolters, Y. Miroshnychenko, P. Grangier, and A. Browaeys, “Entanglement of two individual neutral atoms using rydberg blockade,” *Phys. Rev. Lett.*, vol. 104, p. 010502, 2010.
- [8] D. Kielpinski, “A small trapped-ion quantum register,” *J. Opt. B: Quantum Semiclass. Opt.*, vol. 5, pp. R121–R135, 2011.
- [9] J. R. Petta, A. C. Johnson, J. M. Taylor, E. A. Laird, A. Yacoby, M. D. Lukin, C. M. Marcus, M. P. Hanson, and A. C. Gossard, “Coherent manipulation of coupled electron spins in semiconductor quantum dots,” *Science*, vol. 309, no. 5744, pp. 2180–2184, 2005.

- [10] P. Neumann, N. Mizuochi, F. Rempp, P. Hemmer, H. Watanabe, S. Yamasaki, V. Jacques, T. Gaebel, F. Jelezko, and J. Wrachtrup, “Multipartite entanglement among single spins in diamond,” *Science*, vol. 320, no. 5881, pp. 1326–1329, 2008.
- [11] I. Buluta, S. Ashhab, and F. Nori, “Natural and artificial atoms for quantum computation,” *Reports on Progress in Physics*, vol. 74, no. 10, p. 104401, 2011.
- [12] D. L. Moehring, M. J. Madsen, K. C. Younge, R. N. Kohn, P. Maunz, L. M. Duan, and C. Monroe, “Quantum networking with photons and trapped atoms (invited),” *J. Opt. Soc. Am. B*, vol. 24, pp. 300–315, 2007.
- [13] J. D. Sterk, *Enhanced light collection from single trapped ions*. PhD thesis, University of Michigan, 2011.
- [14] V. Bužek and M. Hillery, “Quantum copying: Beyond the no-cloning theorem,” *Phys. Rev. A*, vol. 54, pp. 1844–1852, Sep 1996.
- [15] H. J. Briegel, W. Dur, J. I. Cirac, and P. Zoller, “Quantum repeaters: The role of imperfect local operations in quantum communication,” *Phys. Rev. Lett.*, vol. 81, no. 26, pp. 5932–5935, 1998.
- [16] M. Zukowski, A. Zeilinger, M. A. Horne, and A. K. Ekert, “Event-ready-detectors: Bell experiment via entanglement swapping,” *Phys. Rev. Lett.*, vol. 71, pp. 4287–4290, 1993.
- [17] D. L. Moehring, P. Maunz, S. Olmschenk, K. C. Younge, D. N. Matsukevich, L. M. Duan, and C. Monroe, “Entanglement of single-atom quantum bits at a distance,” *Nature*, vol. 449, pp. 68–71, 2007.
- [18] P. Maunz, S. Olmschenk, D. Hayes, D. N. Matsukevich, L. M. Duan, and C. Monroe, “Heralded quantum gate between remote quantum memories,” *Phys. Rev. Lett.*, vol. 102, p. 250502, 2009.
- [19] P. Kumar, “Quantum frequency conversion,” *Optics Letters*, vol. 15, pp. 1476–1478, 1990.
- [20] H. Takesue, “Single-photon frequency down-conversion experiment,” *Phys. Rev. A*, vol. 82, p. 013833, 2010.
- [21] R. W. Boyd, *Nonlinear Optics*. Academic Press, 2008.
- [22] W. P. Risk, T. R. Gosnell, and A. V. Nurmikko, *Compact blue-green lasers*. Cambridge University Press, 2003.
- [23] S. Borri, P. Cancio, P. D. Natale, G. Giusfredi, D. Mazzotti, and F. Tamassia, “Power-boosted difference-frequency source for high-resolution infrared spectroscopy,” *Appl. Phys. B*, vol. 76, pp. 473–477, 2003.

- [24] P. Canarelli, Z. Benko, R. Curl, and F. K. Tittel, “Continuous-wave infrared laser spectrometer based on difference frequency generation in aggas2 for high-resolution spectroscopy,” *JOSA B*, vol. 9, pp. 197–202, 1992.
- [25] T. W. Tukker, C. Otto, and J. Greve, “Elliptical-focusing effect on parametric oscillation and downconversion,” *JOSA B*, vol. 15, pp. 2455–2462, 1998.
- [26] G. D. Boyd and D. A. Kleinman, “Parametric interaction of focused gaussian light beams,” *Journal of Applied Physics*, vol. 39, no. 8, pp. 3597–3640, 1968.
- [27] N. Curtz, R. Thew, C. Simon, N. Gisin, and H. Zbinden, “Coherent frequency-down-conversion interface for quantum repeaters,” *Optics Express*, vol. 18, pp. 22099–22104, 2010.
- [28] M. A. Albota, *Single-Photon Frequency Upconversion for Long-Distance Quantum Teleportation and Communication*. PhD thesis, Massachusetts Institute of Technology, June 2006.
- [29] J. Pelc, *Frequency conversion of single photons: physics, devices, and applications*. PhD thesis, Stanford, 2012.
- [30] K. Shinozaki, C. Xu, H. Sasaki, and T. Kamijoh, “A comparison of optical second-harmonic generation efficiency using bessel and gaussian beams in bulk crystals,” *Optics Comm.*, vol. 133, pp. 300–304, 1997.
- [31] K. Nakamura, J. Kurz, K. Parameswaran, and M. M. Fejer, “Periodic poling of magnesium-oxide-doped lithium niobate,” *Journal of Applied Physics*, vol. 91, pp. 4528–4534, 2002.
- [32] D. H. Jundt, “Temperature-dependent sellmeier equation for the index of refraction, n_e , in congruent lithium niobate,” *Optics Letters*, vol. 22, pp. 1553–1555, 1997.
- [33] I. Shoji, T. Kondo, A. Kitamoto, M. Shirane, and R. Ito, “Absolute scale of second-order nonlinear-optical coefficients,” *J. Opt. Soc. Am. B*, vol. 14, no. 9, pp. 2268–2294, 1997.
- [34] M. M. Fejer, A. Magel, D. H. Jundt, and R. L. Byer, “Quasi-phase-matched second harmonic generation: tuning and tolerances,” *IEEE Jour. of Quant. Elec.*, vol. 28, no. 11, pp. 2631–2654, 1992.
- [35] V. Magni, “Optimum beams for efficient frequency mixing in crystals with second order nonlinearity,” *Optics Communications*, vol. 184, no. 1-4, pp. 245 – 255, 2000.

- [36] A. Ridah, P. Bourson, M. D. Fontana, and G. Malovichko, “The composition dependence of the raman spectrum and new assignment of the phonons in LiNbO_3 ,” *J. Phys. Condens. Matter*, vol. 9, pp. 9687 – 9693, 1997.
- [37] P. Hermet, M. Veithen, and P. Ghosez, “First-principles calculations of the non-linear optical susceptibilities and raman scattering spectra of lithium niobate,” *J. Phys. Condens. Matter*, vol. 19, p. 456202, 2007.
- [38] R. F. Schaufele and M. J. Weber, “Raman scattering by lithium niobate,” *Phys. Rev.*, vol. 152, no. 2, pp. 705–708, 1966.
- [39] K. Lengyel, L. Kovacs, A. Peter, K. Polgar, and G. Corradi, “The effect of stoichiometry and mg doping on the raman spectra of $\text{LiNbO}_3:\text{Mg}$ crystals,” *Appl. Phys. B*, vol. 87, pp. 317–322, 2007.
- [40] J. G. Scott, S. Mailis, C. L. Sones, and R. W. Eason, “A raman study of single-crystal congruent lithium niobate following electric-field repoling,” *Appl. Phys. A*, vol. 79, pp. 691–696, 2004.